RESEARCH PAPER

Element-specific study of the coupled magneto-structural and magneto-electronic properties of CoNi nanoarrays

**Chao-Yao Yang · Yuan-Chieh Tseng ·
Hong-Ji Lin**

Abstract The magneto-structural (MS) and magneto-electronic (ME) effects, as well as their coupling relationship, were investigated in electroless-plated (EL) $Co_{0.5}Ni_{0.5}$ arrays treated by post N_2 annealing and in situ field plating. Separately and combined, these two treatments have been widely employed to improve the properties of magnetic nanostructures. This work aimed to discriminate between treatments with respect to electronic and structural properties, and magnetic degrees of freedom of $Co_{0.5}Ni_{0.5}$ nanostructures. The field-plated sample exhibited a strong MS–ME coupling due to magneto-crystalline anisotropy (MCA), arising from a FCC (111) preferred orientation with lattice planes stacking orthogonally to the long axial direction of the arrays. A large coercivity was observed in this structure, arising from high magnetic stability. X-ray magnetic circular dichroism revealed that magnetization was enhanced primarily by Co magnetism, while the field-plated sample underwent a MS/ME transition with corresponding increase of the plating field. Conversely, the heat-treated sample comprised isotropically oriented nanocrystals approximately 20 ± 3 nm in diameter, coated with an oxidation layer (approximately 5 ± 2 nm thick). The absence of MCA in these samples ensured a weak MS–ME coupling. Although the Ni magnetization of heat-treated samples remained close to that of the field-plated sample, the Co constituent exhibited CoO and Co_3O_4 phases in addition to the metallic state. By contrast, the Co constituent of the field-plated sample was mainly metallic. The lack of MCA, combined with a complex Co magnetic state, appears responsible for the divergent macroscopic magnetic behaviors of the heat-treated and the field-plated samples. By isolating changes in local magnetic moments of Ni and Co, we gained a fundamental understanding of the effects of post-N_2 annealing and field plating on CoNi. Such knowledge may assist researches in improving the magnetic properties of bimetallic nanostructures.

Keywords Nanoarrays · CoNi · XMCD · Electroless · Magneto-crystalline anisotropy

C.-Y. Yang · Y.-C. Tseng (✉)
Department of Materials Science & Engineering,
National Chiao Tung University, 1001 Ta Hsueh Road,
Hsinchu 30010, Taiwan, ROC
e-mail: yctseng21@mail.nctu.edu.tw

H.-J. Lin
National Synchrotron Radiation Research Center, Taiwan,
101 Hsin Ann Road, Hsinchu Science Park,
Hsinchu 30076, Taiwan, ROC

Introduction

Co_xNi_{1-x} is ubiquitously used in magnetism studies (Yang et al. 2011; Yamauchi et al. 2004; Sankara et al. 2003; Qin et al. 2002; Ohtake et al. 2009;

Pané et al. 2007; Gómez et al. 2005; Gálvez et al. 2010; Kuepper et al. 2011). Having a naturally high atomic moment and coercivity, Co promotes the magnetization and magnetic hardness of Ni to satisfy technological needs (Yang et al. 2011; Yamauchi et al. 2004; Sankara et al. 2003). Given its ubiquity, Co_xNi_{1-x} is expected to exhibit high chemical stability in a variety of forms. For example, Co_xNi_{1-x} may be easily deposited onto various substrates (Yang et al. 2011; Ohtake et al. 2009) or embedded into different matrices (Pané et al. 2007; Gómez et al. 2005), providing a means of investigating the interactions between ferromagnetic (FM) and (non)-magnetic systems. In addition, the magnetic/electronic properties of Co_xNi_{1-x} can be tailored to a particular application by varying the Co_xNi_{1-x} composition (Gálvez et al. 2010; Liot and Abrikosov 2009). As researchers devote ever-more attention to nanotechnology, they seek a fundamental knowledge of low-dimensional magnetic behaviors. The synthesis of various Co_xNi_{1-x} nanostructures has become a popular approach for investigating these behaviors. However, unlike its Fe_xNi_{1-x} counterpart, whose anomalous (invar) transition has been well-studied in both bulk and nanostructure (Glaubitz et al. 2011; Liot and Abrikosov 2009), Co_xNi_{1-x} is understood only as an alloy with tunable magnetic properties.

Our recent studies on electroless (EL)-plated magnetic nanoarrays have revealed a strong coupling between microstructure and magnetism (Yang et al. 2011; Liu et al. 2009; Huang et al. 2011). We also discovered that although both heat treatment and Co-doping promotes magnetic ordering by enhancing the microstructural ordering of the Ni arrays, the latter treatment alone generates an electronic-dependent transition (Yang et al. 2011). This suggests that Co induces an additional magneto-electronic (ME) effect that complements the original magneto-structural (MS) effect in the undoped Ni. While a few studies have demonstrated microstructural and magnetic correlations in thin films and nanostructures of Co_xNi_{1-x} (Ohtake et al. 2009; Ung et al. 2005; Wu et al. 2010), our results suggest that Co modifies the properties of Ni in rather more complex ways, underlain by the ME effect. This work is an extension of our previous study (Yang et al. 2011), in which Co-induced effects were clearly demonstrated. Here we focus on the nanoscale properties of Co_xNi_{1-x}, namely, its electronic and magnetic coupling, and structural degrees of freedom.

To this end, we investigated two sets of Co_xNi_{1-x} arrays of a fixed x value ($x = 0.5$); one subjected to various magnetic fields during the EL-plating and the other treated by thermal annealing in a N_2 atmosphere. Both treatments, separately or in combination, have been shown to improve the properties of magnetic materials (Liu et al. 2009; Huang et al. 2011; Marín et al. 2006; Ito et al. 2007; Shamaila et al. 2009). By applying the two treatments independently, we could contrast the MS and ME effects, and also examine their coupling strength. Since the fabricated Co_xNi_{1-x} were highly ordered, magneto-crystalline anisotropy (MCA) was established along the long axial direction of the field-plated arrays, rendering their MS effect and coupled ME significantly different from those of the heat-treated samples. Our separate-treatment approach contrasts starkly with studies utilizing magnetic field annealing (Marín et al. 2006; Ito et al. 2007; Shamaila et al. 2009), in which the individual effects of the MCA and thermal energy on the properties of the materials were vaguely determined. Using X-ray absorption spectroscopy (XAS), X-ray magnetic circular dichroism (XMCD), transmission electron microscopy (TEM), and X-ray diffraction (XRD), we investigated the properties of Co_xNi_{1-x} undergoing different structural/electronic transitions. XAS and XMCD collectively provided an element-specific, electronic-sensitive probe of the changing magnetism and oxidation states of the two constituents (Co, Ni) as the transition progressed. Because the Co and Ni contents in the material were equal, any transition-induced changes of magnetic or oxidation states from either constituent would alter the overall properties, enabling a direct correlation between the MS and ME effects. Both effects, as well as the coupling between them, differed markedly between the Co_xNi_{1-x} treated by annealing and field plating. Comparing these results, the interplays between Co and Ni under the influences of the two treatments could be elucidated.

Experimental section

Co_xNi_{1-x} nanoarrays ($x = 0.5$) were fabricated within an anodic alumina oxide (AAO) template, adopting an EL-plating technique. An AAO template with the pore size $\sim 100 \pm 5$ nm was sensitized and activated by a $SnCl_2/HCl$ solution (40 g L^{-1} $SnCl_2$ + 3 ml l^{-1} HCl) and a $PdCl_2/HCl$ solution (0.15 g L^{-1}

$PdCl_2$ + 3 ml l^{-1} HCl) prior to the EL-plating process. The plating solution used in this work consisted of $CoSiO_4$ (0.025 M), $NiSO_4$ (0.025 M), $(NH_4)_2SO_4$ (0.5 M), and NaH_2PO_2 (0.3 M), where $CoSiO_4$, and $NiSO_4$ served as the main Co and Ni sources. $(NH_4)_2SO_4$ and NaH_2PO_2 served as buffer agent and the main reduction agent, respectively. Since the samples investigated in this work were composition-independent, they are hereafter designated CoNi, and their Curie temperatures were found to be around 1,100 K. Field-plated CoNi samples were prepared by applying an external field of 0, 0.2, or 0.4 T along the long axial direction of the arrays in the presence of the AAO during plating, and were designated MFP0, MFP2, and MFP4, respectively. The heat-treated sample was prepared by thermally annealing the plated CoNi at 600 °C for 3 h in an N_2 atmosphere, using a tube furnace in the presence of AAO. This sample was designated as TA. To enable quantitative comparison between the magnetic properties of the samples, sample dimensions were precisely and identically controlled by the AAO. The compositions of both CoNi sets were verified by energy-dispersive X-ray spectrometry (EDX) to ensure that the Co(Ni) concentration had not altered under the treatments. The surface morphology of the CoNi was probed by a scanning electron microscope (SEM, JSM 6500F) operated at 15 kV. Atomic-scale images were obtained by high resolution transmission electron microscope (HRTEM, JEM-2100F operated at 200 keV). Structural characterizations were confirmed by Cu kα XRD. Magnetic properties were analyzed by a vibrating sample magnetometer (VSM), with magnetic hysteresis (M–H) loops taken along the long axial direction of the arrays. XAS spectra were collected over Co/Ni L_{II} and L_{III} edges with a total electron yield mode (TEY) at beamline of 11A, at the National Synchrotron Radiation Research Center (NSRRC), Taiwan. At the same facility, XMCD signals (for probing the spin-polarization state of the arrays) were obtained by reversing the X-ray helicity. All XMCD signals were recorded at room temperature, under a magnetic field of 1 T. Combining these two techniques probed the electronic occupations of Co and Ni in the vicinity of their Fermi levels, in an element-specific manner. Following data collection, the orbital (m_{orb}) and spin (m_{spin}) moments of the samples were derived from the XAS and XMCD spectra by sum-rules analysis (Chen et al. 1995).

Results and discussion

Figure 1a, b shows the cross-sectional and top-viewed SEM images, respectively, of the AAO template before plating. The template is composed of numerous hollow tubes, each of depth $\sim 300 \pm 5$ nm and diameter $\sim 100 \pm 5$ nm. These tube dimensions determined the aspect-ratio (approximately 3) of the CoNi arrays. The free-standing nature of the plated CoNi arrays (with AAO removed) is apparent in their cross-sectional and top-viewed SEM images (Fig. 1c, d, respectively).

Figure 2a–c displays HRTEM images of MFP0, TA, and MFP4, respectively. The HRTEM of MFP0 (Fig. 2a) reveals that the CoNi microstructure was unaffected by field plating and heat treatment. The microstructure contains nanocrystals (NCs) of average diameter approximately 5 ± 2 nm. The microstructure is of short range order, characterized by randomly oriented NCs embedded in an amorphous matrix (Yang et al. 2011; Liu et al. 2009). However, the TA and MFP4 microstructures, shown in Fig. 2b, c, respectively, are more crystalline than that of the MFP0. The annealing process facilitated the growth of TA NCs by expanding the NCs to approximately 20 ± 3 nm in diameter. Nevertheless, the TA exhibits no preferred orientation; mis-oriented NCs are highlighted in the inset of Fig. 2b. The MFP4 microstructure, on the other hand, is highly oriented, with specific lattice planes stacking orthogonally to the axial direction throughout the arrays, as shown in Fig. 2c. The lattice spacing, estimated as 2.03 Å, corresponds to the (111) inter-plane spacing of CoNi FCC (Kumah et al. 2007; Niu et al. 2004). The one-way orientation of MFP4 is universal, as evidenced from a HRTEM taken within another region of the array (Fig. 2c, inset). Similar results were obtained for MFP2 (data not shown). The preferred orientation appears to arise from the magnetic field applied during the plating process, as previously observed by Niu et al. (2004) in field-synthesized Ni nanoparticles. Since [111] is the axis along which CoNi FCC is most easily magnetized (Tang et al. 2007), this phenomenon must arise from aligning the magnetic moment in a specific crystallographic direction, to acquire minimum energy for spin-orbit coupling (Spaldin 2003). Thus, the crystallization mechanism of the MFP4 differs that of the TA (whose crystal development is limited and isotropic). The differences in crystallization mechanism ensure different crystallographic properties of the two samples.
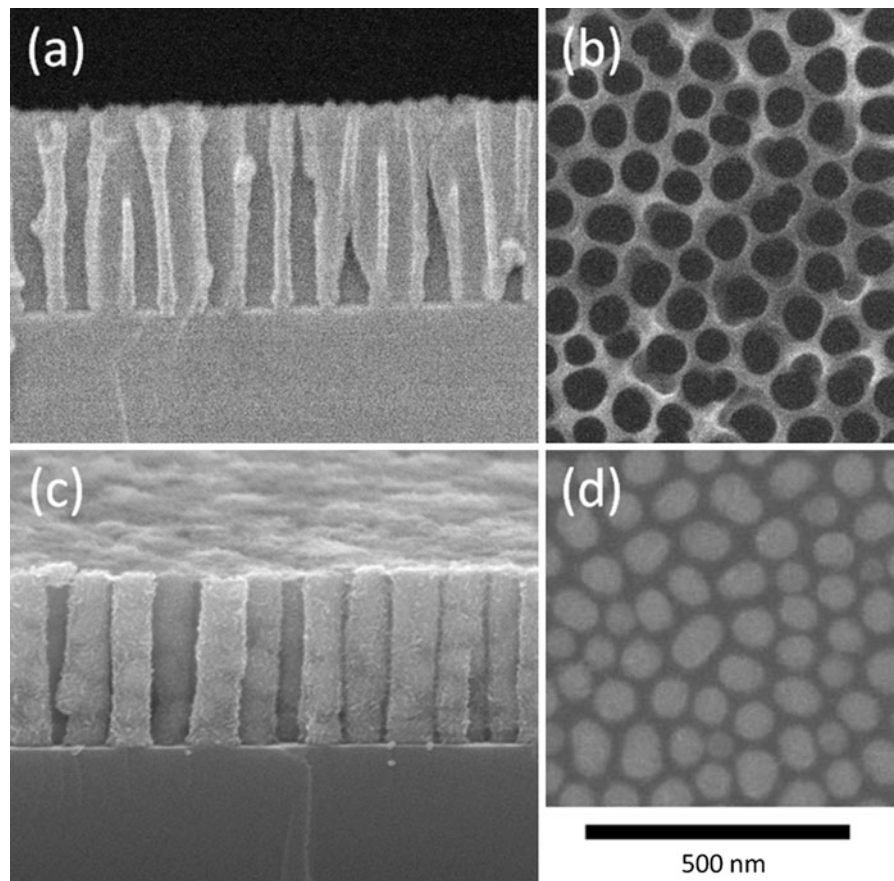
Fig. 1 **a** SEM cross-sectional and **b** top-viewed images of the AAO template. **c** SEM cross-sectional and **d** top-viewed images of CoNi arrays after the removal of the AAO. *Scale bar* shown in **d** is applied to all subfigures

For example, the XRD pattern of MFP4 reveals mainly FCC (111) orientation (Fig. 3a), while that of TA shows an additional index of (200), arising from the isotropic orientation. Since FCC [111] is the preferential crystallographic direction of MFP4, a highly favored MCA is expected in the MFP4 rather than in the TA.

This surmise is validated by the M–H loops of the two samples, displayed in Fig. 3b, c for TA and MFP4, respectively. Because the M–H loops were taken along the long axial direction of the arrays, they reflect the stability of the magnetic moment along the [111] direction in MFP4. The coercivity (H_c) of MFP4 is relatively large ($\sim$850 Oe), indicating that the moment/crystal alignment is energetically favorable (Spaldin 2003). Conversely, the coercivity of TA is much reduced ($H_c \sim$ 300 Oe), suggesting a mixture of favorable and unfavorable MCAs in this structure. Summarizing the above results, we infer that the distinct effects of field plating and heat treatment

processes on the CoNi result from dissimilar MS transitions. The thermal energy applied to TA favors isotropic crystallization but compromises the magnetic stability (Qin et al. 2002). However, the magnetic field applied to MFP4 simultaneously rotates the moments and the (111) plane, due to MS coupling in the CoNi. Thus, the crystallization mechanism of MFP4 is dominated by MCA, and the magnetic properties are considerably different from those of TA.

The presence of MCA in MFP4 also appears responsible for the strong MS effect observed in MFP4 (relative to TA). To further understand the MS effect and its relationship with plating-field strength, we collected XRD and M–H loops for the MFP0, MFP2, and MFP4 samples. XRD and M–H loops are presented in Fig. 4a, b, respectively. The FCC (111) peak intensity increases with increasing plating field, suggesting progressive crystallization as the MCA is increasingly favored (Fig. 4a). As shown in Fig. 4b,
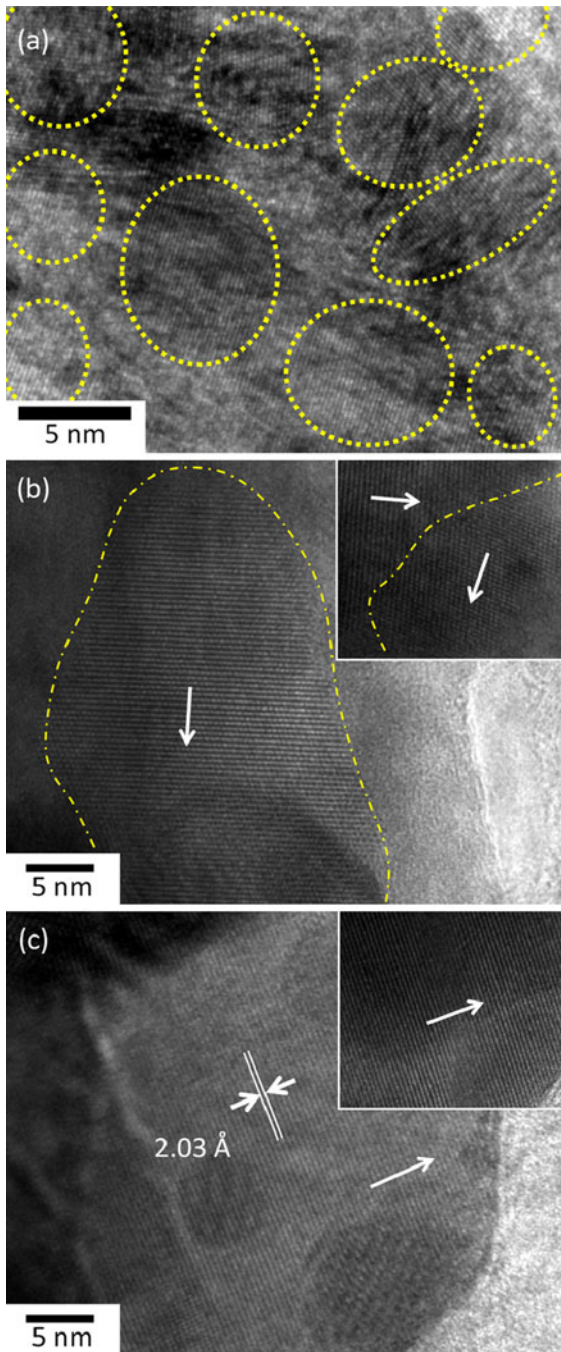
◄**Fig. 2** HRTEM images of **a** MFP0, **b** TA, and **c** MFP4. In **a**, the NCs are highlighted by the *yellow dashed circles*. In **b**, the *arrow* in the main figure indicates the orientation direction of the NC. *Inset* of **b** provides two adjacent NCs with their orientations denoted by the respective *arrows*. In **c**, the *arrow* in the main figure indicates the orientation of the CoNi FCC (111), as well as the long axial direction of the arrays. *Inset* of **c** provides a HRTEM image taken from another part of MFP4, where the *arrow* indicates the same information as it does in the main figure. (Color figure online)

intermediate phase induced by the reducing agent NaH_2PO_2 in the plating process, also increases with increasing plating field (see Figs. 3a, 4a). Press et al. (1987) reported that the nickel constituent of Ni_3P is substantially demagnetized by Pp–Nid orbital hybridization, rendering the Ni_3P a paramagnetic phase (PM). In our study, the Ni_3P-PM appears to be coupled to a specific crystallographic direction, as evidenced by its magnetic field dependency in the XRD intensity data (Fig. 4a). However, we consider that the Ni_3P, by virtue of its PM nature, introduces a limited FM component to the main CoNi FM phase, especially in terms of H_c, and therefore exerts negligible influence on the MS effects observed in CoNi.

Although the magnetic properties of field-plated and heat-treated CoNi are clearly distinguished by differences in their MS effects, the situation from a micromagnetism perspective is more complicated. In particular, the local magnetic moments of Co and Ni may vary independently under treatment. By contrast, the study of Niu et al. (2004) focused on a single constituent (nickel). We attempt to clarify this situation by presenting separate XAS and XMCD results from Ni and Co.

Figure 5a shows L_{II} and L_{III} XAS of Ni in the field-dependent (MFP0, MFP2, MFP4) and heat-treated (TA) samples. Nominally, the XAS is independent of the treatments, and the peak splittings at both absorption edges are attributable to Ni oxidation. However, since metallic nickel possesses an exchange-split d orbital, unoccupied states exist near the L_{II} and L_{III} edges, with appreciable shoulders at 4 and 6 eV above the respective white lines (Chen et al. 1990). In addition, Ni_3P possesses states around the same energy ranges (Blanchard et al. 2008). Together, these factors mask the oxidation state of Ni and obscure the comparison. To detect spectral changes, the first derivatives of all Ni XAS spectra must be compared against that of a standard NiO spectrum, as shown in Fig. 5b. These

the magnetic properties are substantially altered as plating field rises, with the saturation magnetization (main panel), H_c (upper inset) and squareness (M_r/M_s, lower inset) all becoming more pronounced.

Interestingly, the XRD intensity of the Ni_3P phase (Sankara et al. 2003; Press et al. 1987), an unavoidable

Fig. 3 **a** XRD comparison for MFP4 and TA. M–H loops of **b** TA and **c** MFP4. Both M–H loops were normalized to respective M_S
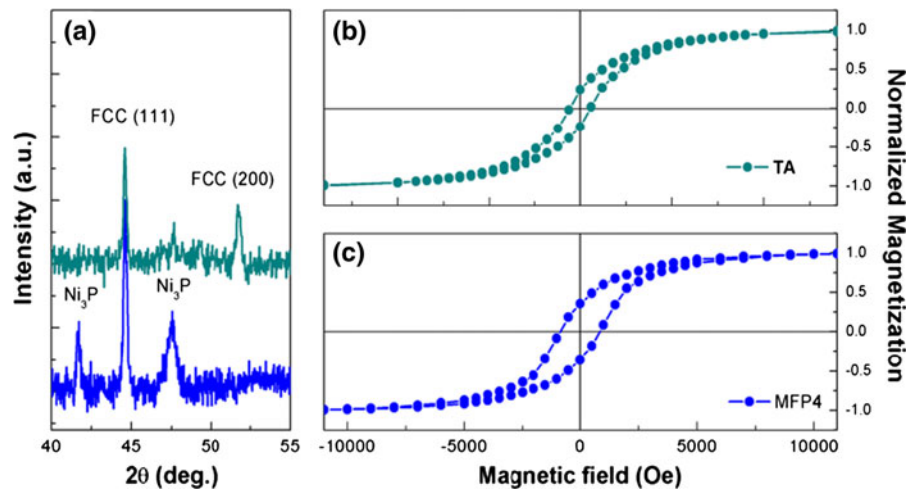

Fig. 4 **a** XRD patterns and **b** M–H loops for field-plated CoNi. All the M–H loops were normalized to the M_S of MFP4. *Upper inset* of **b** is the zoom-in information of the H_c. *Lower inset* of **b** is the squareness (M_r/M_s) comparison for the three samples
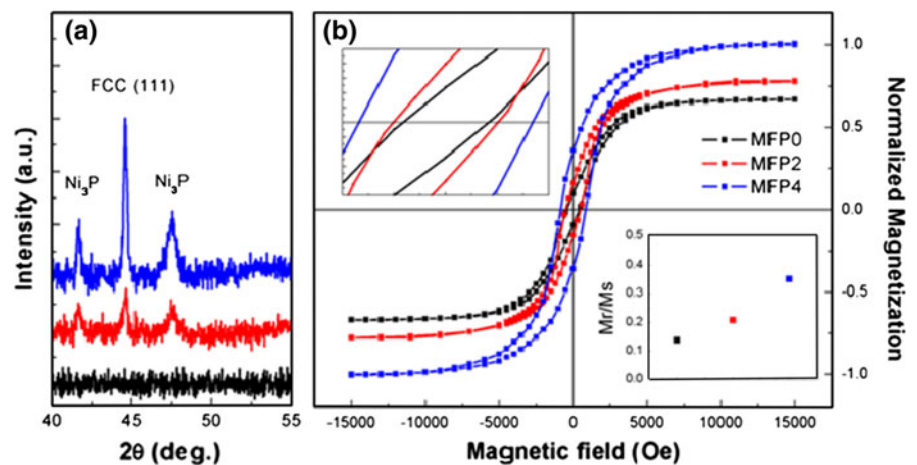
results suggest that oxidation of the investigated samples deviates considerably from that of pure NiO. However, as highlighted in the inset of Fig. 5b, the XAS of the Ni constituent of TA approaches that of pure NiO, suggesting that the state of Ni electronically depends on the MS transition, even if only minimally.
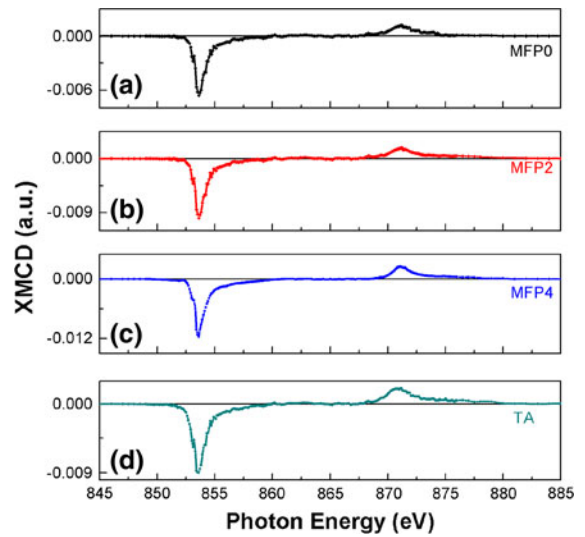
Oxidation occurred primarily at array surfaces exposed to the atmosphere. This phenomenon can readily be probed by surface-sensitive XAS in TEY mode, as suggested by Huang et al. (2011) HRTEM and XAS fitting results (see Fig. 8) revealed that oxidation indeed occurs at the surrounding array surfaces, while the CoNi remains largely unaltered within the array. This is validated by two further findings. First, with regard to Ni, the XMCD signals (Fig. 6) and FM-like M–H loops (Figs. 3b, c, 4b), are clear for all samples, indicating that Ni in the magnetized samples exists

largely as a metal. NiO is a known antiferromagnet (Mandal et al. 2009) whose M–H is heavily suppressed and whose XMCD is unobtainable except in the event of large moment canting. Secondly, the HRTEM spectra (Fig. 2) of crystalline CoNi should be homogeneous. Around the array surface, however, homogeneity is lost in the TA (Fig. 2b), and a microstructure similar to that of a Ni–NiO core–shell structure, as reported by Hsu et al. (2012) and Lo et al. (2011) is observed. In the former studies, the Ni–NiO structures were prepared by annealing the Ni arrays at 350 °C for 15–30 min in an O_2 environment, with no AAO protection. In our study, although the TA was prepared in the presence of the AAO under an N_2 atmosphere, a higher annealing temperature (600 °C) and a prolonged annealing time (3 h) may have encouraged surface oxidation at regions of close contact between the arrays and the oxygen-
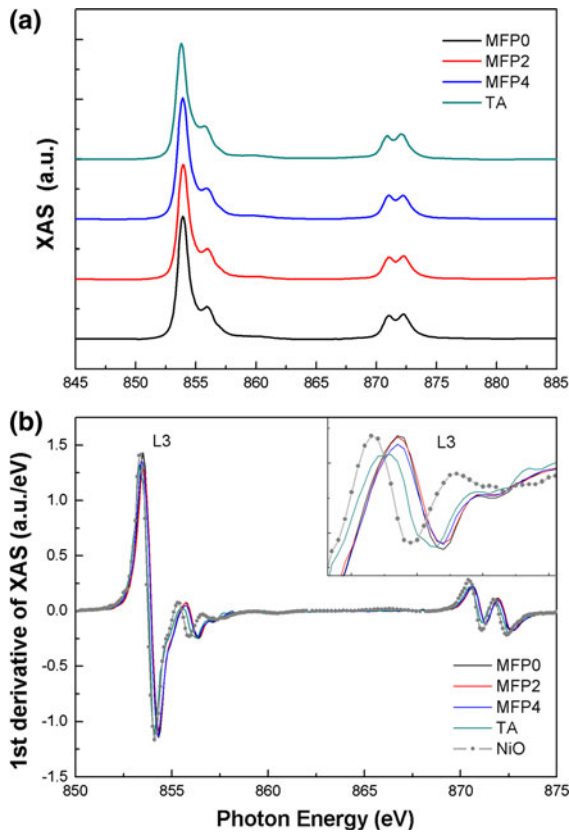
Fig. 5 **a** Normalized Ni XAS spectra for TA, MFP0, MFP2, and MFP4. **b** First derivatives of the spectra corresponding to those presented in **a**. The first derivative of a standard NiO is given in **b** for comparison. *Inset* of **b** is the zoom-in information for the comparison around the L_{III} edge

Fig. 6 Ni XMCD spectra for **a** MFP0, **b** MFP2, **c** MFP4, and **d** TA. All the XMCD spectra were normalized to the integrations of respective XAS spectra. Note that the XMCD intensity scalings (y-axis) are different

abundant AAO. We also note the absence of surface inhomogeneity in the field-plated samples. This finding confirms that the thin oxidation layer generated by the annealing process caused surface inhomogeneity in the TA samples. Surface homogeneity is markedly improved in MFP4. In this process, the continuous stacking of lattice planes on the array surface inhibits Ni(Co) oxidation. Consequently, Ni and Co are less oxidized when the CoNi undergoes a MCA-dominant transition, as will be discussed later. To summarize, the high surface-to-volume ratio of the arrays renders some oxidation inevitable, a problem that is widespread in nanostructure fabrication. However, oxidation level varies with constituent as well as treatment (Co and Ni oxidation are markedly different, as explained below). Such properties must be considered by researchers employing the two common treatments in bimetallic nanostructure fabrication.

Although treatment produces negligible effect on the XAS of Ni, the XMCD signal, whose magnitude reflects the strength of the local magnetic moment, is heavily dependent on treatment. To illustrate this point, the XMCD spectra of Fig. 5a are normalized and compared in Fig. 6a–d. The XMCD intensity of Ni in the field-plated samples follows a trend similar to that of the M–H loops (Fig. 4b). This implies that the MS and ME of Ni are fully coupled by the MCA predominance. For the TA sample, on the other hand, the Ni XMCD intensity is larger than that of the MFP0, but smaller than that of the MFP4. This phenomenon is consistent with the saturation magnetizations of the samples. It appears that the microscopic behavior of Ni mirrors the macroscopic response of the arrays, unlike the situation for Co (see below). The behavior of Ni in the arrays, and the overall properties of the arrays, could also be explored from the size of the NCs. For example, crystallinity is a key indicator of the FM of EL-plated arrays (Yang et al. 2011; Huang et al. 2011); thus the NC size, which is related directly to crystallinity, might correlate to Ni magnetism. Based on this idea, we regard the Ni magnetism of TA to lie between that of MFP0 and MFP4.

We now consider the XAS/XMCD spectra of Co. Figure 7 shows the Co L_{II} and L_{III} XAS spectra for all samples. Unlike the case for Ni, Co oxidation is treatment-dependent, as observed by contrasting the

two main peaks of the L_{III} edge. Yet like Ni, Co signals are detected in the XMCD spectra of all samples, indicating that partial oxidation has occurred (Fig. 9). To further elucidate the oxidation state of Co, the Co L_{III} XAS spectra were fitted by properly weighting the metallic (Yang et al. 2011), CoO (Lee et al. 2010), and Co_3O_4 (Singh et al. 2009) states. The results for MFP4 and TA are presented in Fig. 8a, b, respectively. In depicting the chemical state of cobalt, the L_{III} edge is considered as a better fingerprint than the L_{II} edge. During fitting, the XAS of Co in MFP4 was found to be representative of the entire field-treated series. Thus, subsequent Co analysis on field-treated samples is presented for MFP4 alone. Co remains mainly metallic in the field-plated sample (~ 70 %), but is heavily oxidized in the TA, appearing as both Co^{2+} and Co^{3+} ionic forms. Heat treatment may favor the formation of CoO (2^+) or Co_3O_4 (2^+ and 3^+) phases at the surface (Lee et al. 2010; Singh et al. 2009). The oxidation potential of Co is higher than that of Ni (http://www.siliconfareast.com/ox_potential.htm); thus Co oxidation is readily acquired at the L_{III} edge. Since both Co and Ni are partially oxidized in our study, we may question whether the surface-sensitive TEY-mode of XAS provided the surface rather than the bulk properties of the NCs. A cursory check of our previous work will alleviate these concerns (Yang et al. 2011). In our previous study, metallic Co in low Co-doped (6 %) Ni arrays was probed by TEY-mode XAS. Therefore, the moderate oxidation level (30 %) detected in the field-plated samples cannot be attributed to technical problems. Instead, it is an intrinsic property of increased Co content, as more Co atoms are exposed to the surface.

Figures 9a–e show the Co XMCD spectra of the three field-plated samples (a–c) and the TA (d), and a metallic Co spectrum (e) for comparison. The Co XMCD spectra of the field-plated samples behave similarly to those of their Ni counterparts; the signal increases with increasing plating-field due to the MCA effect. The XMCD line-shape is independent of field strength and exhibits metallic characteristics, suggesting that Co contributes a significant FM component to the overall magnetization, while undergoing a MCA-dominant MS transition. On the other hand, the Co XMCD spectrum of TA is noisy due to the complex oxidation state (Fig. 8b). The oscillations in the XMCD likely arise from interactions between the AFM and FM phases at the surface and interior,
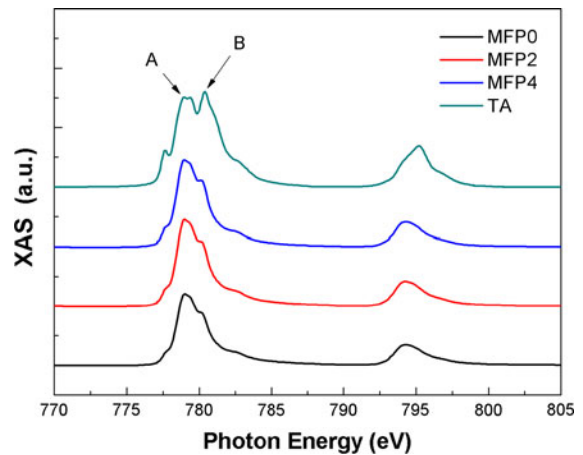
Fig. 7 Normalized Co XAS spectra for MFP0, MFP2, MFP4, and TA. *A* and *B arrows* indicate the two main peaks at L_{III} edge of TA, at which the contrast between the two peaks is remarkably different than those of the field-plated samples
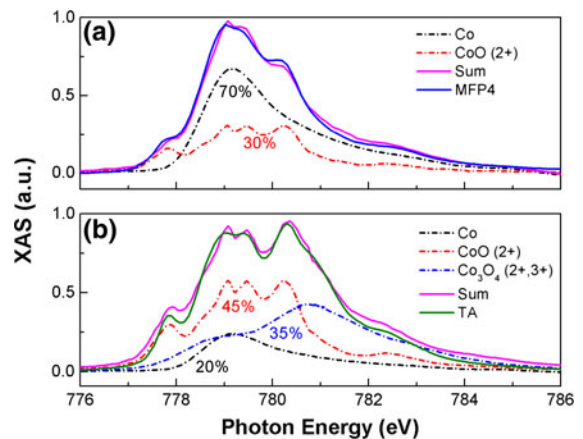
Fig. 8 Co XAS fittings of **a** MFP4 and **b** TA over L_{III} edge, with various states [metallic Co, CoO (2^+) and Co_3O_4 (2^+, 3^+), cited from Blanchard et al. 2008, Spaldin 2003, and Shamaila et al. 2001, respectively] properly weighted

respectively. We note that AFM is produced by surface oxidation states (CoO, Co_3O_4) (Golosovsky et al. 2006; Mousavand et al. 2009), while the FM phase is generated by the central metallic state. Oscillatory XMCD spectra have been reported in several studies of oxide-shell and metallic-core structures (Imperia et al. 2005; Jiménez-Villacorta et al. 2011; Mulders et al. 2009). The magnitude of oscillation depends on the fractions of, and the exchange interactions between, the oxide and metallic phases.
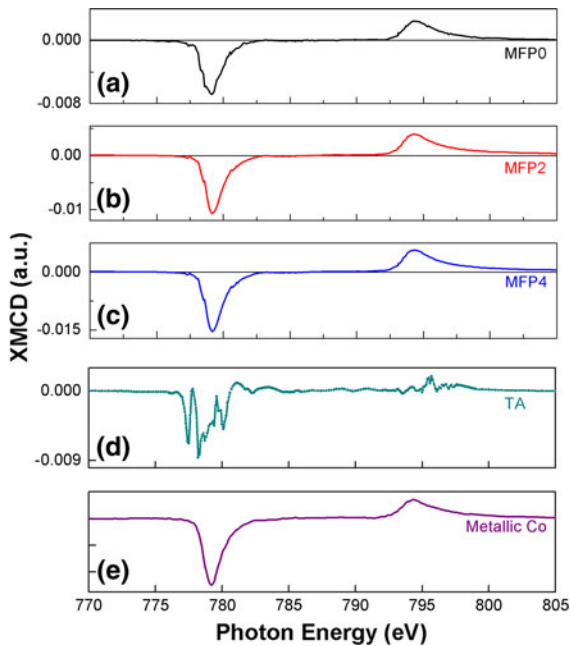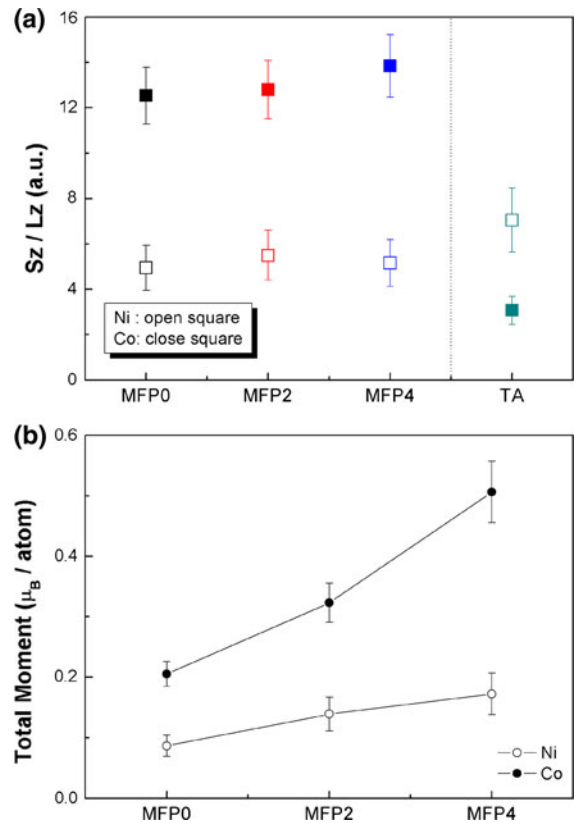
Fig. 9 Co XMCD spectra for **a** MFP0, **b** MFP2, **c** MFP4, **d** TA, **e** metallic Co. All the XMCD spectra were normalized to the integrations of respective XAS. In **e**, the metallic Co is only for a line-shape comparison so its XMCD intensity is not scaled

Fig. 10 a S_z/L_z ratios for Ni (*open squares*) and Co (*close squares*) gained from sum-rule analyses, for MFP0 (*black*), MFP2 (*red*), MFP4 (*blue*), and TA (*green*). *Vertical dashed line* separates the field-plated samples (*left-hand side*) and the heat-treated sample (*right-hand side*), for the purpose of clarity. **b** Sum-rule estimated total magnetisms ($S_z + L_z$) of Co and Ni for the field-plated samples. (Color figure online)

Finally, the micro-magnetisms of the two constituents subjected to both treatments were explored by sum-rule analyses. The results are shown in Fig. 10. In Fig. 10a, the comparison is based on the ratio of m_{spin}/m_{orb} (S_z/L_z), to eliminate possible errors arising from different n_{3d}, given that the oxidation states differ between field-plated and heat-treated samples. We emphasize that for the field-plated samples, all L_z and S_z of both constituents increase as plating field increases, as can be inferred from Figs. 6 and 9. However, since L_z and S_z increase similarly, the change in S_z/L_z is imperceptible. In the TA sample, the micro-magnetic behavior of Ni is similar to that in the field-plated samples, but the behavior of Co deviates significantly, due to complex oxidation processes. In summary, the strongly coupled MS–ME ensures that Co and Ni behave similarly in field-plated samples, while the weakly coupled MS–ME in TA leads to dissimilar behaviors of its constituents.

Although Co and Ni behave similarly in the field-plate samples, we can determine their individual contributions to the total magnetization as plating field is increased, by calculating ($S_z + L_z$) of both constituents (see Fig. 10b). Since the Co and Ni oxidation states are independent of the plating field, and XMCD show predominantly metallic states, possible errors introduced by use of n_{3d} are excluded, and a qualitative comparison is meaningful. We observe that, in the MCA-dominant case, in which MS–ME are strongly coupled, the trends observed in Fig. 4b are attributable to the substantial enhancement of Co magnetism, because Ni magnetization is rather insensitive to plating field.

Conclusions

Using XAS/XMCD, TEM, XRD, and VSM, we have investigated the MS and ME effects and their coupling, in heat-treated and field-plated CoNi arrays.

The heat-treated sample exhibited randomly oriented NCs, and the arrays were coated by an oxidation layer. By contrast, the field-plated samples strongly preferred the FCC (111) orientation. The FCC (111) effectively stabilized the magnetic moments of these samples, resulting in pronounced coercivities and saturation magnetizations, whose magnitudes depended on the magnitude of the plating field. Furthermore, both Co and Ni magnetisms were enhanced with increasing plating field, but the former dominated the latter in the overall magnetization. The Ni in heat-treated and field-plated samples behaved similarly, but the behavior of Co deviated largely under the different treatments. In the TA sample, discrete behaviors of Ni and Co were attributable to complex oxidation states of Co and lack of the MCA effect. Post-annealing and field plating significantly influenced the MS and ME properties of CoNi NCs. The Co and Ni magnetizations were isolated from the CoNi, and information derived from the results was related to the probed crystallographic and microstructural properties of the NCs. The results of this study could promote the effective use of the two treatments, thereby improving the magnetic properties of bimetallic nanostructures.

References

Blanchard PE, Grosvenor AP, Cavell RG, Mar A (2008) X-ray photoelectron and absorption spectroscopy of metal-rich phosphides M2P and M3P (M = Cr-Ni). Chem Mater 20:7081–7088

Chen CT, Sette F, Ma Y, Modesti S (1990) Soft-X-ray magnetic circular dichroism at the $L_{2,\,3}$ edges of nickel. Phys Rev B 42:7262–7265

Chen CT, Idzerda YU, Lin HJ, Smith NV, Meigs F, Chaban E, Ho GH, Pellegrin E, Sette F (1995) Experimental confirmation of the X-ray magnetic circular dichroism sum rules for iron and cobalt. Phys Rev Lett 75:152–155

Gálvez N, Valero E, Ceolin M, Trasobares S, López-Haro M, Calvino JJ, Domínguez-Vera JM (2010) A bioinspired approach to the synthesis of bimetallic CoNi nanoparticles. Inorg Chem 49:1705–1711

Glaubitz B, Buschhorn S, Brüssing F, Abrudan R, Zabel H (2011) Development of magnetic moments in $Fe_{1-x}Ni_x$-alloys. J Phys 23:254210

Golosovsky IV, Mirebeau I, André G, Tovar M, Tobbens DM, Kurdyukov DA, Kumzerov YA (2006) Magnetic phase transition in a nanostructured antiferromagnet CoO embedded in porous glass. Phys Solid State 48:2130–2133

Gómez E, Pané S, Vallés E (2005) Magnetic composites CoNi–barium ferrite prepared by electrodeposition. Electrochem Commun 7:1225–1231

Hsu HC, Lo CC, Tseng YC (2012) Competing magnetic interactions and interfacial frozen-spins in Ni–NiO core–shell nano-rods. J Appl Phys 111:063919

Huang CC, Lo CC, Tseng YC, Liu CM, Chen C (2011) Magnetostructural phase transition in electroless-plated Ni nanoarrays. J Appl Phys 109:113905

Imperia P, Schmitz D, Maletta H, Sobal NS, Giersig M (2005) Effect of Ar^+ and H^+ etching on the magnetic properties of Co/CoO core–shell nanoparticles. Phys Rev B 72:014448

Ito N, Michels A, Kohlbrecher J, Garitaonandia JS, Suzuki K, Cashion JD (2007) Effect of magnetic field annealing on the soft magnetic properties of nanocrystalline materials. J Magn Magn Mater 316:458–461

Jiménez-Villacorta F, Prieto C, Huttel Y, Telling ND, van der Laan G (2011) X-ray magnetic circular dichroism study of the blocking process in nanostructurediron-iron oxide core–shell systems. Phys Rev B 84:172404

Kuepper K, Benoit DM, Wiedwald U, Mögele F, Meyering A, Neumann M, Kappler JP, Joly L, Weidle S, Rieger B, Ziemann P (2011) Precise chemical, electronic, and magnetic structure of binuclear complexes studied by means of X-ray spectroscopies and theoretical methods. J Phys Chem C 115:25030–25039

Kumah DP, Cebollada A, Clavero C, García-Martín JM, Skuza JR, Lukaszew RA, Clarke R (2007) Optimizing the planar structure of (111) Au/Co/Au trilayers. J Phys D 40:2699–2704

Lee YJ, de Jong MP, Jansen R (2010) Magnetism and heterogeneity of Co in anatase $Co:TiO_2$ magnetic semiconductor. Appl Phys Lett 96:082506

Liot F, Abrikosov IA (2009) Local magnetovolume effects in $Fe_{65}Ni_{35}$ alloys. Phys Rev B 79:014202

Liu CM, Tseng YC, Chen C, Hsu MC, Chao TY, Cheng YT (2009) Superparamagnetic and ferromagnetic Ni nanorod arrays fabricated on Si substrates using electroless deposition. Nanotechnology 20:415703

Lo CC, Huang CC, Liu CM, Chen C, Kuo CY, Lin HJ, Tseng YC (2011) Magnetic properties of electroless-deposited Ni and Ni–NiO core–shell nano-arrays. J Magn Magn Mater 323:1950–1953

Mandal S, Banerjee S, Menon KSR (2009) Core–shell model of the vacancy concentration and magnetic behavior for antiferromagnetic nanoparticle. Phys Rev B 80:214420

Marín P, López M, Vlad A, Hernando A, Ruiz-González ML, González-Calbet JM (2006) Magnetic field driving custom assembly in (FeCo) nanocrystals. Appl Phys Lett 89:033508

Mousavand T, Naka T, Sato K, Ohara S, Umetsu M, Takami S, Nakane T, Matsushita A, Adschiri T (2009) Crystal size and magnetic field effects in Co_3O_4 antiferromagnetic nanocrystals. Phys Rev B 79:144411

Mulders AM, Loosvelt H, Fraile Rodríguez A, Popova E, Konishi T, Temst K, Karis O, Arvanitis D, Van Haesendonck C (2009) On the interface magnetism of thin oxidized Co films: orbital and spin moments. J Phys 21:124211

Niu H, Chen Q, Ning M, Jia Y, Wang X (2004) Synthesis and one-dimensional self-assembly of acicular nickel nanocrystallites under magnetic fields. J Phys Chem B 108:3996–3999

Ohtake M, Nukaga Y, Sato Y, Kirino F, Futamoto M (2009) Epitaxial growth of fcc-Co_xNi_{100-x} thin films on MgO(110) single-crystal substrates. J Appl Phys 106:123921

Pané S, Gómez E, García-Amorós J, Velasco D, Vallés E (2007) First stages of barium ferrite microparticles entrapment in the electrodeposition of CoNi films. J Electroanal Chem 604:41–47

Press MR, Khanna SN, Jena P (1987) Electronic structure, magnetic behavior, and stability of Ni-P. Phys Rev B 36:5446–5453

Qin DH, Wang CW, Sun QY, Li HL (2002) The effects of annealing on the structure and magnetic properties of CoNi patterned nanowire arrays. Appl Phys A 74:761–765

Sankara N, Selvakumar S, Stephen A (2003) Electroless Ni–Co–P ternary alloy deposits: preparation and characteristics. Surf Coat Technol 172:298–307

Shamaila S, Sharif R, Chen JY, Liu HR, Han XF (2009) Magnetic field annealing dependent magnetic properties of $Co_{90}Pt_{10}$ nanowire arrays. J Magn Magn Mater 321:3984–3989

Singh AP, Kumar R, Thakur P, Brookes NB, Chae KH, Choi WK (2009) NEXAFS and XMCD studies of single-phase Co doped ZnO thin films. J Phys 21:185005

Spaldin N (2003) Magnetic materials: fundamentals and device applications, Chap 10. Cambridge University Press, Cambridge, p 124

Tang XT, Wang GC, Shima M (2007) Magnetic layer thickness dependence of magnetization reversal in electrodeposited CoNi/Cu multilayer nanowires. J Magn Magn Mater 309:188–196

Ung D, Viau C, Ricolleau C, Warmont F, Gredin P, Fiévet F (2005) CoNi nanowires synthesized by heterogeneous nucleation in liquid polyol. Adv Mater 17:338–344

Wu M, Liu G, Li M, Dai P, Ma Y, Zhang L (2010) Magnetic field-assisted solvothermal assembly of one-dimensional nanostructures of Ni–Co alloy nanoparticles. J Alloy Compd 491:689–693

http://www.siliconfareast.com/ox_potential.htm

Yamauchi Y, Yokoshima T, Momma T, Osaka T, Kuroda K (2004) Fabrication of magnetic mesostructured nickel–cobalt alloys from lyotropic liquid crystalline media by electroless deposition. J Mater Chem 14:2935–2940

Yang CY, Huang CC, Tseng YC, Liu CM, Chen C, Lin HJ (2011) Coupled microstructural and magnetic transition in Co-doped Ni nanoarrays. J Appl Phys 110:073913